Electronic Supplementary Material (ESI) for Lab on a Chip.
This journal is © The Royal Society of Chemistry 2019

Electronic Supplementary Information (ESI) for

Thermographic Characterization of Thin Liquid Films Formation and Evaporation in Microchannels

Meisam Habibi Matin, Abdolreza Fazeli, Saeed Moghaddam*

*Correspondence to: saeedmog@ufl.edu

This file includes:

Methods
Supplementary Text
Figs. S1 to S3

Methods

Fabrication of the microfluidic chip

Figure S1 shows the microfabrication sequence. First, 330 nm-thick silicon oxide layers were thermally grown on both sides of an n-type <100> silicon wafer (Fig. S1a). The oxide layers serve as electrical insulation layers between sputtered sensors and bare silicon substrate. Next, a standard lithography process with 1-µm-thick LOR 3A and 1.5-µm-thick positive photoresist AZ1512 is performed and the photoresist is developed in AZ 300MIF to pattern the sensor area. This is followed by the fabrication of bottom sensor array through sputter deposition of a 50 nm Ti adhesion layer, 100 nm of Pt layer and 200 nm of Au layer followed by the lift-off process. Subsequently, Au is wet etched from the serpentine shape part of the sensor array (Fig. S1a). For the lift-off process, the wafer is soaked in PRS-3000 for 5 minutes to lift the metals off from the areas with no sensor pattern. Now the bottom layer sensor is fabricated. Then, a thin layer (10µm) of SU8 film was spun coated on the bottom sensor array and subsequently hard baked for 1 hour at 180°C (Fig. S1b). Next, following the standard lithography process (the same as bottom layer sensors), the top sensor array was fabricated through the sputter deposition of 50 nm Ti adhesion layer, 100 nm of Pt layer and 200 nm of Au layer followed by lift-off process and subsequent Au etching from within the sensor area of the top sensor array (Fig. S1c). Thus, the bottom layer sensor was built on the silicon substrate and the top layer sensor is sputtered on the SU8.

It should be noted that the adhesion of a metal layer to a hard baked SU8 is inherently weak. To improve the adhesion strength, the surface of SU8 layer was etched by O_2/CF_4 reactive ion etching (RIE) with O_2 flow rate of 40 sccm, CF_4 flow rate of 10 sccm, pressure of 25 mT and power of 100 W to increase its roughness. Before doing next steps the sensors needed to be protected. Therefore, a 10 nm thick layer of TiO2 was sputter deposited on the sensor areas by using standard lithography of a 3µm negative photoresist (AZ nLOF) followed by standard lift-off process in PRS-3000.

In the next step, a blanket Al layer with a thickness of 500 nm was sputter deposited on the SU8 film followed by patterning and etching of the Al layer for the bond pads of the bottom sensor array as well as a 10 µm diameter window at the center of the pulsed function micro heater (Fig. S1d). Using the patterned Al layer, the SU8 layer was etched by O_2/CF_4 RIE (Fig. S1e). The Al layer was subsequently etched away from the surface by through wet etching process. The inlet and outlet ports were dry etched from the backside of the Si wafer using the deep reactive ion etching (DRIE) process (Fig. S1f). Then, a cavity 300 nm in diameter was fabricated using a focused ion beam (FIB) milling machine at the center of the pulsed function micro heater (Fig. S1h) for generation of the bubbles. A 75-µm-thick SU8 film was then spun coated on the wafer, patterned using appropriate mask and developed in the SU8 developer to form the side walls of the microchannel. In the final step, a Polydimethylsiloxane (PDMS) layer was plasma bonded to the SU8 layer to seal the microchannel (Fig. S1i). Finally the device is diced by a dicing saw to have the appropriate size for wire bonding and then wire bonded to a custom made PCB.

Supplementary Text

Numerical simulation of heat transfer events in phase I

The simulation domain consists of SU-8 and FC-72 layers and considers the evaporation in the FC-72 domain. The initial conditions for the liquid thickness and temperature profile in solid and liquid domains were defined as:

$$T_{SU8}(y,t=0) = T_s + q''_{S.Ph} \times {}^{y}/_{k_{SU8}} \tag{s-1}$$

$$T_{FC-72}(y,t=0) = T_{inter} + q''_{S.Ph} \times {}^{y}/_{k_{FC-72}} \tag{s-2}$$

$$\delta_0 = \delta(t=0) = \delta_{Ph-II} + (\delta_0 - \delta_{Ph-II}) = \delta_{Ph-II} + \int_0^{\tau} {}^{q''}/_{\rho h_{fg}}\, dt \tag{s-3}$$

where τ denotes the overall time of phase I. In the simulation process, the flow rate in the liquid layer and thus the convective mode of heat transfer is considered negligible (as shown in the "hydrodynamic study of the liquid layer" section, the liquid flow under the bubble is almost insignificant) and the energy and mass balance equations for a transient conduction problem with evaporating media are developed and solved for this study, as follows:

SU8 domain:

$$\frac{\partial^2 T}{\partial y^2} = \frac{1}{\alpha} \times \frac{\partial T}{\partial t}, 0 < y < 10, 0 < t < \tau \tag{s-4}$$

FC-72 domain:

$$\frac{\partial^2 T}{\partial y^2} = \frac{1}{\alpha} \times \frac{\partial T}{\partial t}, 10 < y < 10 + \delta(t), 0 < t < \tau \tag{s-5}$$

$$\delta(t) = \delta_0 - \int_0^{t} {}^{q''(t)}/_{\rho h_{fg}}\, dt,\ q''(t) = k_{SU8} \times \left.\frac{\partial T}{\partial y}\right|_{y=10} \tag{s-6}$$

A Matlab code was written to solve the energy equation. Its results for a specific case study are presented in Fig. 4A in the manuscript. Less than 10% relative error was observed between the numerical and experimental results, and it was shown that, while the surface temperature is reducing, the heat input into the liquid layer is rising.

<u>Hydrodynamic study of the liquid layer</u>

A portion of the liquid layer flow in the elongated bubble regime can be identified as shear-driven motion induced by the vapor core in the center of the microchannel. The startup problem can be written as:

Vapor core domain:

$$\frac{\partial P}{\partial x} = \mu_{vapor}\left(\frac{\partial^2 U_x}{\partial x^2} + \frac{\partial^2 U_x}{\partial y^2}\right) \tag{s-7}$$

Liquid layer domain:

$$0 = \mu_{liquid}\left(\frac{\partial^2 U_x}{\partial x^2} + \frac{\partial^2 U_x}{\partial y^2}\right) \tag{s-8}$$

and at the interface ($y = \delta(t)$)

$$\mu \left.\frac{\partial U_x}{\partial y}\right|_{vapor} = \mu \left.\frac{\partial U_x}{\partial y}\right|_{liquid}, \quad U_x|_{vapor} = U_x|_{liquid} \tag{s-9}$$

These equations were numerically solved for different liquid layer thicknesses and vapor velocities and the contribution of liquid layer flow to evaporation mass flux was calculated as:

$$C_f = {}^{\rho_{liquid} U_{x,liquid} A_{liquid}}/_{\dot{m}_{evap.}} \tag{s-10}$$

where $\dot{m}_{evap.} = q'' \times A_{sensor} / h_{fg}$. The value of C_f for different experiments conducted in this study never exceeded 10% of the evaporation mass flux, which indicates the insignificance of the shear-driven flow in this flow configuration (Fig. S2).

Capillary-driven flow of liquid layer

Unlike shear-driven flows, capillary-induced flow of liquids has been regarded as a feasible and effective mechanism to facilitate liquid delivery to the thin film. In this method, the change in radius of curvature at the liquid-vapor interface generates the capillary pressure ($P_c = 2\sigma/R$), which causes wicking of the liquid ($\dot{m} = \rho KA/\mu L_{wick} \times P_c$). Capillary flow in microchannels can be triggered under different conditions. The most common technique to induce wicking of liquid involves utilization of micro/nano-structures. As liquid evaporates from within the structure, the interface curvature adjusts itself such that liquid flows toward the evaporating interface and rewets the heated surface; alternatively, the capillary flow can be developed as a result of the film thickness gradient under a liquid-vapor interface, which generates capillary pressure (and hence liquid flow) even on plain surfaces ($P_c = \sigma \times \frac{\delta''}{[1 + \delta'^2]^{3/2}}$, δ denotes the liquid layer thickness).

For finding the wicking mass flux, $\dot{m}_{w,s}(z) = \frac{\rho}{\mu} \times \frac{dP_c}{dz} \times W \times \delta(z)^3$, the capillary pressure gradient is needed.

The pressure difference between vapor and liquid at the liquid–vapor interface is due to the capillary pressure, and is expressed as:

$$P_c = \sigma K = P_{vap} - P_{liq} \tag{s-11}$$

where $K = \delta''/(1 + \delta'^2)^{1.5}$ is the interfacial curvature and δ' and δ'' are, respectively, the first and second derivatives of thickness with respect to z (Fig. S3).

In view of the very low Reynolds number and the large length-to-height ratio of the thin film, lubrication theory is employed to obtain the pressure gradient. A no-slip boundary condition at the wall and a no-shear boundary condition at the liquid–vapor interface is imposed. Under these assumptions, the liquid pressure gradient dP_{liq}/dz may be related to the wicking mass flux $\dot{m}_{w,s}$. At steady state, the wicking mass flux at a position z is equal to the mean integral of the net evaporative mass flux from the beginning of the film to the local position. The liquid pressure gradient may then be obtained as

$$\frac{dP_{liq}}{dz} = \frac{3\nu}{\delta^3}\int_0^z \dot{m}_w dz \tag{s-12}$$

Assuming the uniform vapor pressure along the meniscus and differentiating Eq. (s-11) with respect to z we get: $dP_c/dz = -dP_{liq}/dz$. We also have:

$$\frac{dP_c}{dz} = \sigma\frac{d}{dz}\left[\delta''/\left(1 + \delta'^2\right)^{1.5}\right] = \sigma\left[\delta'''\left(1 + \delta'^2\right)^{-1.5} - 3\delta'\delta''^2\left(1 + \delta'^2\right)^{-2.5}\right] \tag{s-13}$$

Therefore, combining the equations (s-12) and (s-13), the wicking mass flux can be obtained as:

$$\dot{m}_{w,s} = -\frac{\sigma}{3\nu}\frac{d}{dz}\left[\delta^3\left(\delta'''\left(1 + \delta'^2\right)^{-1.5} - 3\delta'\delta''^2\left(1 + \delta'^2\right)^{-2.5}\right)\right] \tag{s-14}$$

Finding the mass flux requires the curvature of the interface that is the film thickness as a function of z i.e., $\delta(z)$.

Lateral reconstruction of bubble interface

As stated in the manuscript, for the surface heat flux to remain constant, the changes in thickness of liquid layer should be minimal. Therefore, evaporation mass flux should be compensated with the lateral wicking mass flux such that $\dot{m}_{evap.} - \dot{m}_{w,s} \cong 0$.

In this work, we solved the conservation of mass equation along the z-axis as a way to find the local thickness of liquid film in the lateral direction:

$$\dot{m}_{w,s}(z) - \dot{m}_{w,s}(z + dz) = \dot{m}'_{evap}(z) \times dz \quad \text{(s-15)}$$

$$\dot{m}'_{evap}(z) + \partial \dot{m}_{w,s}(z) / \partial z = 0 \quad \text{(s-16)}$$

where wicking ($\dot{m}_{w,s}$) and evaporation ($\dot{m}_{evap.}$) mass fluxes are defined as $\dot{m}_{w,s}(z) = \frac{\rho}{\mu} \times \frac{dP_c}{dz} \times W \times \delta(z)^3$ and $\dot{m}'_{evap.}(z) = \frac{k_f \Delta T}{h_{fg}} \times \frac{W}{\delta(z)}$, respectively.

We then assumed the liquid film thickness profile ($\delta(z)$) in these equations to have a general form of $\delta(z) = \sum_{n=0}^{5} C_n (z/L)^n + A \times (1 - z/L)^k$. The polynomial series term ($\sum_{n=0}^{5} C_n (z/L)^n$) satisfies the boundary conditions at symmetrical points (z=0 and $z \to L$), and the elliptical term ($A \times (1 - z/L)^k$) adjusts the slope of the interface at different locations.

It should be noted that the bubble profile can only be reconstructed precisely if the unknown constants (i.e. $C_0, C_1, C_2, C_3, C_4, C_5, A, k$) are determined in a way that equation (s-14) is satisfied over the entire width of microchannel ($0 < z < L$). Consequently, a modified goal (F) that would achieve those objectives was introduced and then minimized:

$$F = \int_0^z \left[\dot{m}'_{evap}(z) + \partial \dot{m}_{w,s}(z) / \partial z \right]^2 dz \quad \text{(s-17)}$$

Equation (s-17) was minimized via a genetic algorithm (GA) optimization scheme and the calculated constants were used to lay out the liquid/vapor interface (Fig. S3). The maximum difference between the measured evaporation and wicking mass fluxes in this approach was found to be less than 10%, which clearly indicates the role of wicking on maintaining the liquid layer thickness constant.

Non-dimensionalization and scaling of the thermal problem

Over the past years there has been significant research focused on identification and characterization of the parameters that impact two-phase flow in microchannels. Surface heat flux, surface temperature, vapor quality, vapor superficial velocity, surface tension of liquid and vapor phases and viscosity of liquid are among the main parameters that have been heavily studied. It should be noted that conducting the necessary experiments to isolate the impact of each parameter is physically impractical. Therefore, despite considerable research in this area, a universal regime map that can be used to predict the thermal and mass transport properties of two-phase flow in microscale is still missing from the literature.

In this section, we perform an analysis discussing the two-phase flow in microchannels from a macroscopic perspective, which proves the interdependence of these variables and significantly reduces the total number of required experiments. In flow boiling tests inside a

microchannel, for instance, the overall performance of the system can be determined simply by adjusting two parameters. Increasing surface heat flux, selected as one of the driving parameters, causes an elevated evaporation rate inside the microchannel ($q^{"} = \dot{m}_v h_{fg}$) and a faster growth rate of the generated bubbles, which increases vapor quality ($x = \dot{m}_v/\dot{m}$). At constant input mass flow rates ($\dot{m}$) (*i.e.*, second parameter), increasing the vapor quality results in a higher superficial velocity of the bubble ($U_{GS} = x\dot{m}/\rho_G$) and capillary number of the flow ($Ca = \mu U_{GS}/\sigma$), which in turn impacts the thickness of the liquid film (as shown by Bretherton (*1*)). The change in thickness of the liquid layer (δ_V) then dictates the temperature of the surface ($T_s = T_{sat.} + q" \times \left[\delta_V/k_f + \delta_{SU8}/k_{SU8}\right]$). Likewise, decreasing surface heat flux will inversely impact vapor quality, superficial velocity of the bubble and thickness of liquid layer.

In the manuscript, surface temperature and capillary number are selected as the driving parameters due to high controllability and ease of measurement.

Fig. S1.

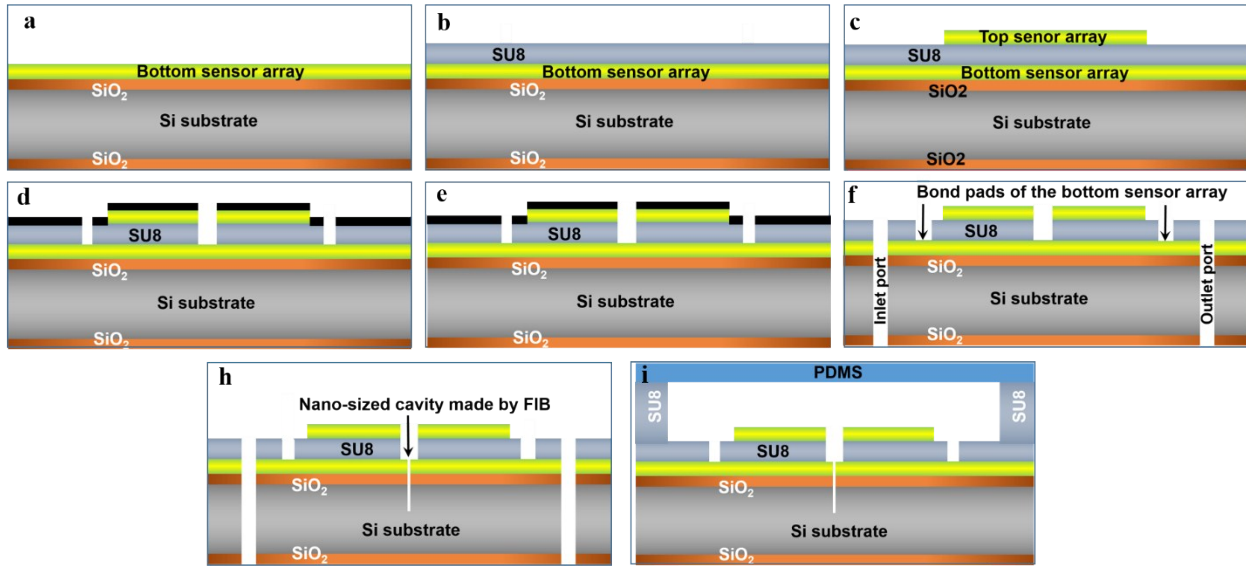

Figure S1: Fabrication sequence of the microfluidic chip, (a) Thermal SiO_2 growth on both sides of Si wafer, deposition of Ti, Pt and Au layers followed by lift-off process and subsequent etching of Au layer from within the bottom sensor array, (b) Spin coating and hard bakig of the SU8 layer, (c) Sputter deposition of the top sensor array, lift-off process and Au etching from within the senor array, (d) Blanket sputter deposition of Al layer, (e) Patterning and etching of the Al layer, (f) O_2/CF_4 RIE etching of SU8 layer, and DRIE etching of the inlet and outlet ports from the backside of the Si wafer, (h) Fabrication of a nano size cavity using a FIB milling tool, and (i) Spin coating of the microchannel side walls and plasma bonding of a PDMS cap to the SU8 microchannel.

Fig. S2.

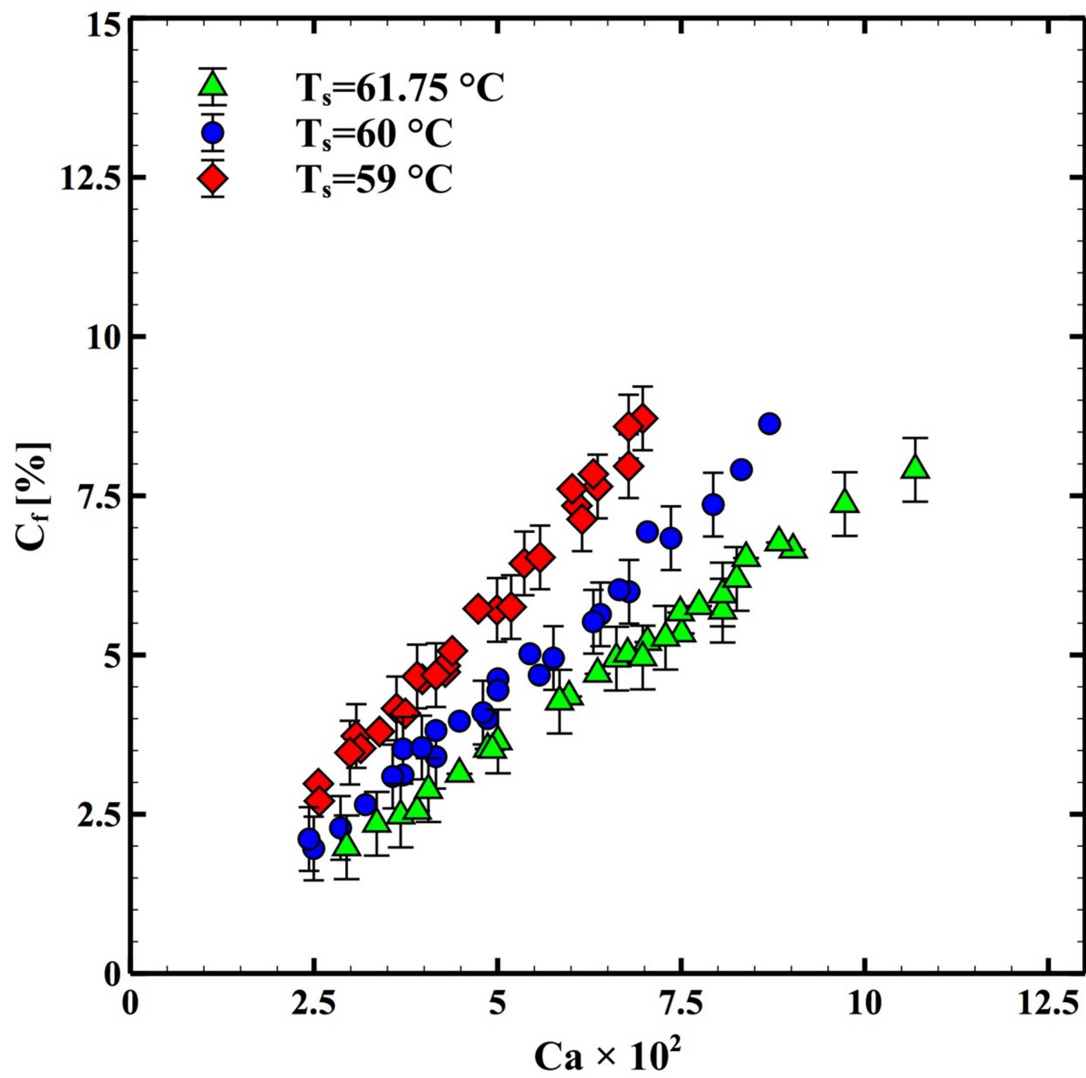

Figure S2: Shear-induced to evaporation liquid flow ratio as a function of capillary number

Fig. S3.

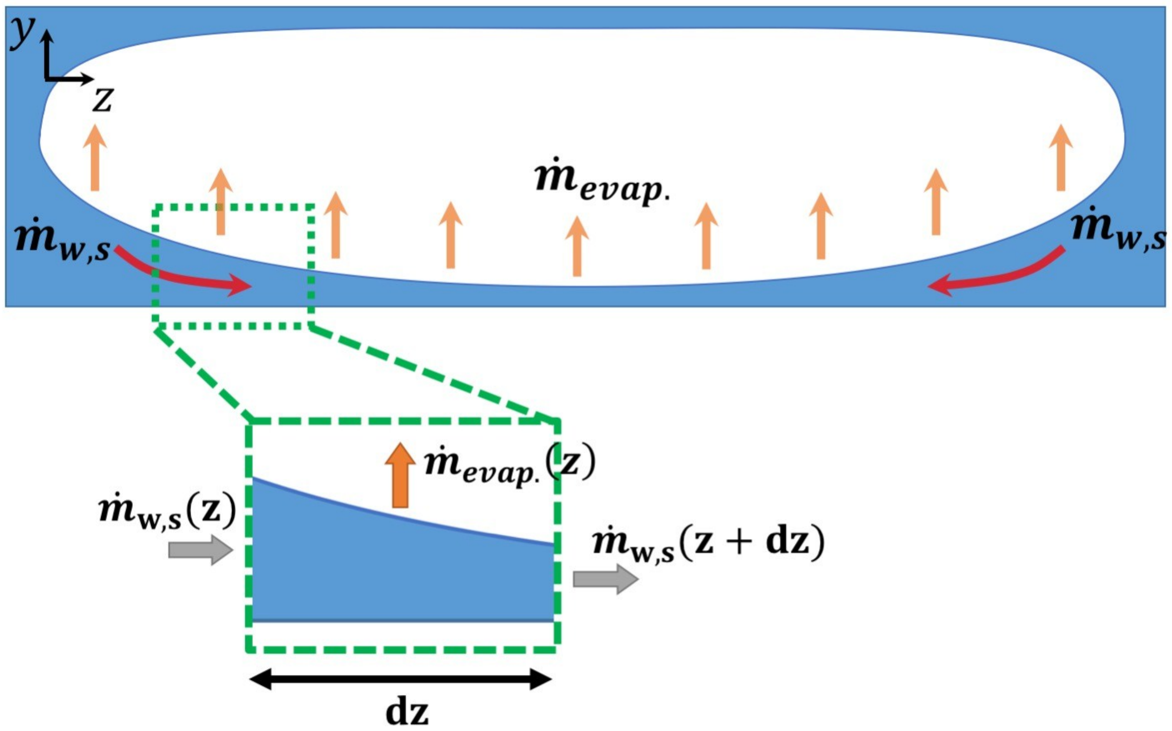

Figure S3: Control volume of liquid/vapor interface